Continental Shelf Research 132 (2017) 38–48

Contents lists available at ScienceDirect

Continental Shelf Research

journal homepage: www.elsevier.com/locate/csr

Is Ekman pumping responsible for the seasonal variation of warm circumpolar deep water in the Amundsen Sea?

T.W. Kim[a], H.K. Ha[b], A.K. Wåhlin[c,*], S.H. Lee[a], C.S. Kim[a], J.H. Lee[d], Y.K. Cho[e]

[a] Korea Polar Research Institute, Incheon 21990 South Korea
[b] Department of Ocean Sciences, Inha University, Incheon 22212 South Korea
[c] Department of Marine Sciences, University of Gothenburg, Gothenburg, Sweden
[d] Korea Institute of Ocean Science and Technology, Ansan 15627 South Korea
[e] School of Earth and Environmental Sciences, Seoul National University, Seoul 08826 South Korea

ARTICLE INFO

Keywords:
Southern Ocean
Ekman transport
Sea ice drift
Amundsen Sea
Circumpolar deep water
Antarctic winter water
Wind stress
Surface stress
Marginal ice zone

ABSTRACT

Ekman pumping induced by horizontally varying wind and sea ice drift is examined as an explanation for observed seasonal variation of the warm layer thickness of circumpolar deep water on the Amundsen Sea continental shelf. Spatial and temporal variation of the warm layer thickness in one of the deep troughs on the shelf (Dotson Trough) was measured during two oceanographic surveys and a two-year mooring deployment. A hydrographic transect from the deep ocean, across the shelf break, and into the trough shows a local elevation of the warm layer at the shelf break. On the shelf, the water flows south-east along the trough, gradually becoming colder and fresher due to mixing with cold water masses. A mooring placed in the trough shows a thicker and warmer layer in February and March (late summer/early autumn) and thinner and colder layer in September, October and November (late winter/early spring). The amplitude of this seasonal variation is up to 60 m. In order to investigate the effects of Ekman pumping, remotely sensed wind (Antarctic Mesoscale Prediction System wind data) and sea ice velocity and concentration (EASE Polar Pathfinder) were used. From the estimated surface stress field, the Ekman transport and Ekman pumping were calculated. At the shelf break, where the warm layer is elevated, the Ekman pumping shows a seasonal variation correlating with the mooring data. Previous studies have not been able to show a correlation between observed wind and bottom temperature, but it is shown here that when sea ice drift is taken into account the Ekman pumping at the outer shelf correlates with bottom temperature in Dotson Trough. The reason why the Ekman pumping varies seasonally at the shelf break appears to be the migration of the ice edge in the expanding polynya in combination with the wind field which on average is westward south of the shelf break.

1. Introduction

According to the Intergovernmental Panel on Climate Change (IPCC, 2013), the West Antarctic Ice Sheet (WAIS) is the largest source of uncertainty in predictions of future sea level rise over the 50–200 year time horizon. The WAIS has experienced a pronounced mass loss in recent decades (Bindschadler, 2006; Rignot et al., 2008; Paolo et al., 2015). This melting of ice into the ocean impacts biogeochemical cycles (Menviel et al., 2010), biological productivity (Hawkings et al., 2014), sea level (Dutton et al., 2015), and sea ice formation (Rignot and Jacobs, 2002). The most rapidly changing region of the West Antarctic is the Amundsen Sea, where the intrusion of relatively warm Circumpolar Deep Water (CDW) onto the continental shelf (Walker et al., 2007; Jenkins et al., 2010; Wåhlin et al., 2010, 2013; Arneborg et al., 2012; Jacobs et al., 2012) may be the reason for observed recent thinning of the floating ice shelves along the coast (e.g. Paolo et al., 2015).

After intruding onto the continental shelf, CDW is modified by mixing with colder water masses, after which it is referred to as modified CDW (MCDW). In situ observations of MCDW flowing towards the ice shelves have been obtained from the deep troughs that connect the outer shelf to the inner shelf basins, e.g. in the north-western branch of the Pine Island Trough (Walker et al., 2007; Assmann et al., 2013), in the main Pine Island Trough (Nakayama et al., 2013; Jacobs et al., 2011) and in the Dotson Trough (Wåhlin et al., 2010, 2013; Arneborg et al., 2012; Ha et al., 2014) (Fig. 1). The temporal variability in Dotson Trough is considerable (Arneborg et al., 2012; Wåhlin et al., 2013; 2015; Ha et al., 2014). On time scales

* Corresponding author.
E-mail address: awahlin@gu.se (A.K. Wåhlin).

http://dx.doi.org/10.1016/j.csr.2016.09.005
Received 2 September 2015; Received in revised form 17 July 2016; Accepted 15 September 2016
Available online 13 November 2016

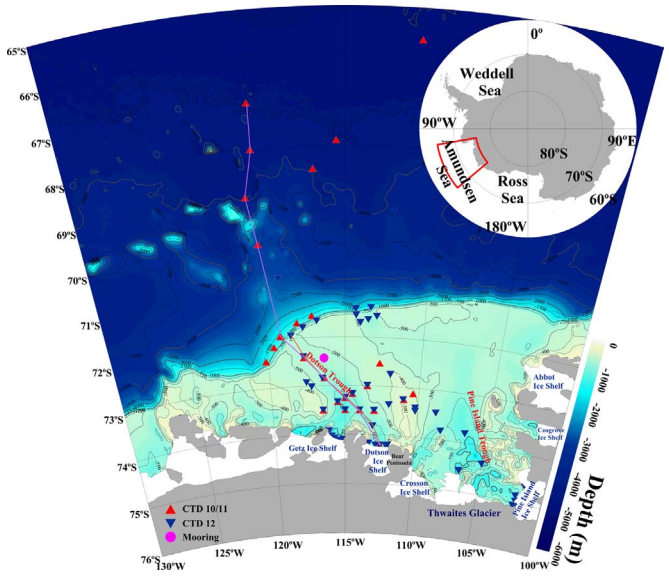

Fig. 1. Map of study area with the CTD stations and the mooring indicated. Red and blue triangles show the CTD stations during the 2010/11 and 2012 Araon expeditions, respectively. The purple circle indicates the mooring station (February, 2010–2012). (For interpretation of the references to color in this figure legend, the reader is referred to the web version of this article.)

shorter than a week, the velocity is characterized by strong barotropic fluctuations that correlate with zonal winds at the shelf break (Wåhlin et al., 2013, 2016; Kalén et al., 2015). The wind drives a clockwise barotropic circulation in the area (Ha et al., 2014; Kalén et al., 2015) and can also set up resonant Rossby waves (Wåhlin et al, 2016). In addition to these short-term fluctuations, there is a persistent south-eastward baroclinic flow of dense warm water (Arneborg et al., 2012) connected to the thickness and density of the warm bottom layer (Wåhlin et al., 2013). However, neither the baroclinic flow nor the bottom temperature correlates with the wind (Wåhlin et al., 2013). This is in contrast to what is seen in model results (e.g. Thoma et al., 2008; Steig et al., 2012) where eastward winds at the shelf break are responsible for transporting warm salty water onto the shelf, a mechanism that has been observed to occur in the Eastern part of the shelf break (Wåhlin et al., 2012). However, since the observed summertime maximum in warm layer thickness in Dotson Trough is not related to any maximum in the eastward winds, it is unlikely that eastward winds alone force the MCDW into the Dotson Trough.

Previous studies that examined the correlation between wind stress and observations of the layer of MCDW in Dotson Trough (Wåhlin et al., 2013) have not accounted for the effect of a sea ice cover, which affects the surface stress. The surface stress induced by a (wind-forced and moving) sea ice cover depends strongly on ice characteristics, and either increased or decreased upwelling or downwelling, compared to an ice-free environment, may result from the presence of the ice (Leppäranta and Omstedt, 1990; Häkkinen, 1986; Carmack and Chapman, 2003; Yang, 2006; Schulze and Pickart, 2012). Very thick ice can take the role of the Ekman layer and veer sharply compared to the wind direction (even more than 45°), while thin ice follows the surface currents. For example, Häkkinen (1986) studied downwelling/upwelling in the marginal ice zone, using a two-dimensional coupled ice-ocean model. The model showed that horizontally homogenous westward winds produced upwelling at the sea ice zone (north of ice edge) and downwelling at the open ocean (south of ice edge) due to the difference between air-ice and air-ocean momentum fluxes. Using satellite and in situ buoy data from the Arctic Ocean, Yang (2006) showed a seasonal variation of heat and salt fluxes induced by Ekman pumping in the Beaufort Sea, and Schulze and Pickart (2012) found that the seasonal variation in upwelling in the Beaufort Sea, induced by the temporal variation of sea ice condition (open water, partial ice and full ice).

Our objective is to examine the combined effect of wind and sea ice drift on the thickness of the layer of MCDW in the western Amundsen continental shelf region, and more specifically to examine if it can explain the seasonal variation of the CDW layer that is observed. This is done by calculating the ocean surface stress, and Ekman pumping, from satellite-derived winds and sea ice drift and comparing these to hydrographic surveys and mooring time series from the Dotson Trough in the Amundsen Sea.

2. Materials and methods

Two oceanographic surveys were conducted by the IBRV *Araon* from 21 December 2010 to 23 January 2011, and from 31 January to 20 March 2012 (Fig. 1). A total of 30 and 52 CTD stations were occupied during the surveys in 2011 and 2012, respectively. At each station, a CTD (SBE 911+) hydrocast was conducted to measure profiles in temperature, pressure, and conductivity. The conductivity sensors were calibrated by Sea-Bird before and after the cruises and salinities were further checked at regular depths by an Autosal

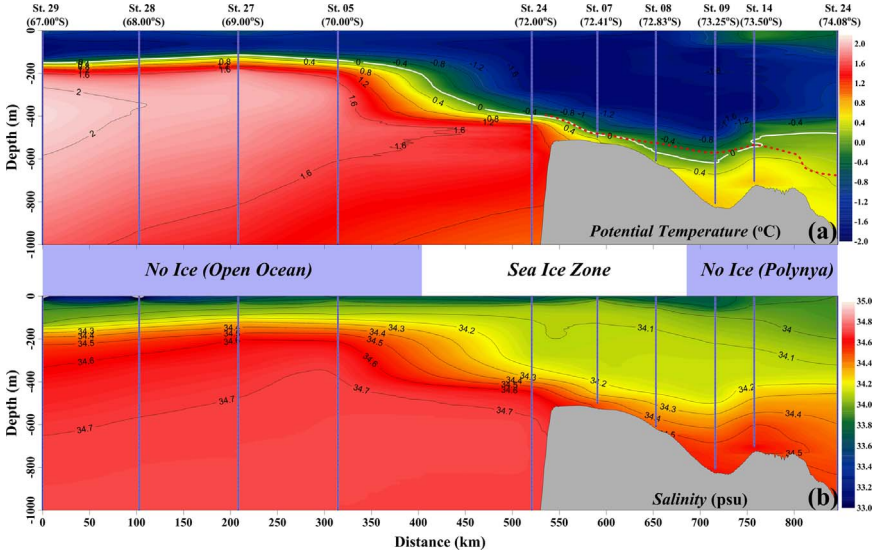

Fig. 2. Cross sections of (a) potential temperature and (b) salinity during the 2011 cruise along a transect from 67° S (left) to the Dotson Ice shelf front (right). Red dashed line in (a) shows the 0 °C isotherm during the 2012 cruise. (For interpretation of the references to color in this figure legend, the reader is referred to the web version of this article.)

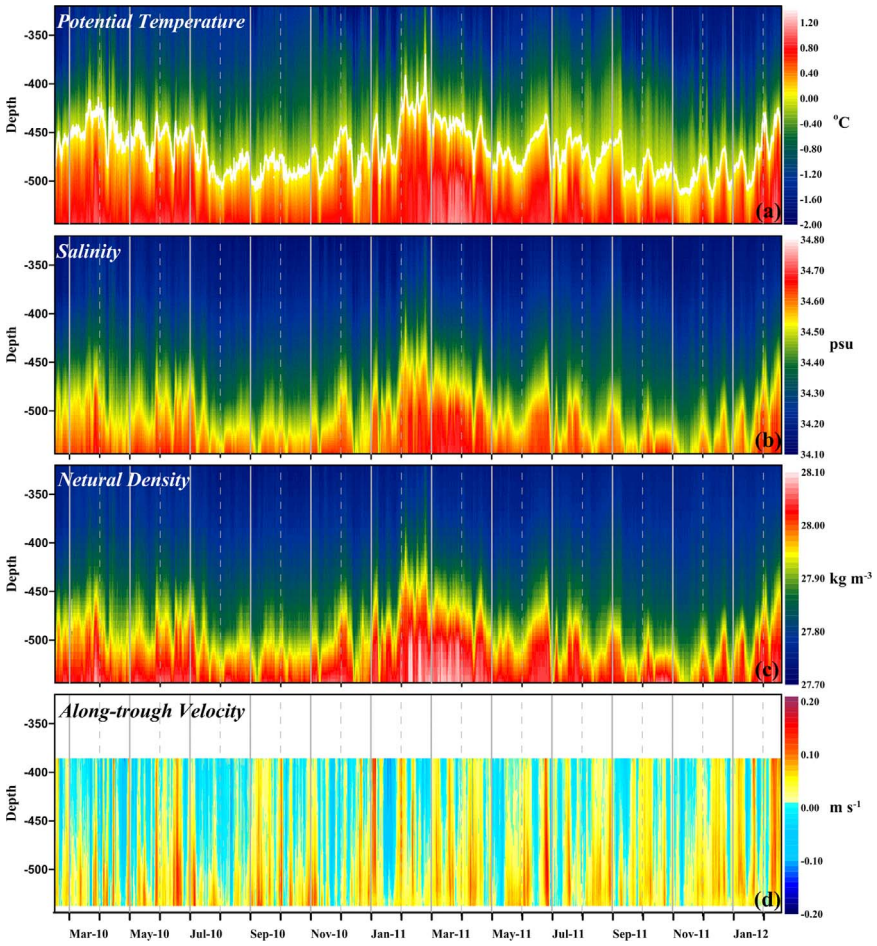

Fig. 3. Time-series of (a) potential temperature, (b) salinity, (c) neutral density and (d) along-trough velocity (defined as velocity projected on 140° with positive values towards the ice shelf) at the mooring station. The white line in (a) shows the 0 °C isotherm.

salinometer (Guildline, 8400B) using water samples. Fig. 2 shows the resulting cross-shelf sections. The temporal variability was observed between February 2010 to 1 March 2012 from a mooring placed at 72.46°S, 116.35°W in the eastern side of Dotson Trough (Fig. 1, see also Wåhlin et al., 2013). The mooring contained an array of Microcats (Seabird, SBE-37SMP) to measure temperature (with an accuracy of 0.002 K) and conductivity (with an accuracy of 0.0003 S m^{-1}); 5 during the first observation period (15 February 2010 to 25 December 2010) and 7 during the second observation period (25 December 2010 to 1 March 2012). An upward-looking 150-kHz Acoustic Doppler Current Profiler (ADCP; RDI) was deployed at the bottom to measure current velocity profiles. The observed velocity data were processed using the WinADCP® software and de-tided using the t_tide toolbox for harmonic analysis (Pawlowicz et al., 2002), which is based on Foreman (1979). Fig. 3 shows the measured time series of temperature, salinity, density and velocity.

Wind data were obtained from the Antarctic Mesoscale Prediction System (AMPS), which employs the Polar WRF (Weather Research and Forecasting Model), a mesoscale model especially adapted for polar regions (Bumbaco et al., 2014) providing gridded wind data at 10 m above the sea surface with a horizontal resolution of 15×15 km and 3 h interval. Sea ice concentration data were obtained from the Nimbus-7 Scanning Multichannel Microwave Radiometer (SMMR, 1979–1987), the Defense Meteorological Satellite Program (DMSP) Special Sensor Microwave/Imager (SSM/I, 1987–2007) and the Special Sensor Microwave Imager/Sounder (SSMIS, 2008-present) (Cavalieri et al., 1996). These provide gridded daily averaged sea ice concentrations with a horizontal resolution of 25×25 km. The sea ice velocity data were obtained from the Polar Pathfinder Daily 25 km EASE-Grid Sea Ice Motion Vectors Version 2 from 1990 to 2011 (Fowler et al., 2013).

Ocean surface stresses at the air-ocean interface (τ_{ao}) were calculated according to

$$\tau_{ao}=(\tau_{ao}^{x},\ \tau_{ao}^{y})= \quad \rho_a C_{D,ao}|\mathbf{W}_{10}|\mathbf{W}_{10}, \tag{1}$$

where (τ_{ao}^{x}, τ_{ao}^{y}) are zonal and meridional components of wind stress, respectively; ρ_a is the air density (1.29 kg m^{-3}) and $\mathbf{W}_{10}$ is the wind velocity vector at 10 m above the sea surface. The drag coefficient between air and ocean ($C_{D,ao}$) was calculated depending on wind speed as follows (Large and Pond, 1981):

$$C_{D,ao}=\begin{cases} 1.2\times10^{-3} & \mathbf{W}_{10}<11 \quad ms^{-1} \\ (0.49+0.065\mathbf{W}_{10})\times10^{-3} & 11\leq\mathbf{W}_{10}\leq25 \quad ms^{-1} \end{cases}. \tag{2}$$

It should be noted that (1) and (2) are, in the absence of data on stratification, based on the assumption that the stratification is stable. In the event of unstable stratification, convection will occur in the surface which will greatly enhance the effective stress. Ocean surface stresses at the ice-ocean interface (τ_{io})were calculated according to

$$\tau_{io}=(\tau_{io}^{x},\ \tau_{io}^{y}) = \quad \rho_w C_{D,io}|\mathbf{U}_{ice}-\mathbf{U}_w|(\mathbf{U}_{ice}-\mathbf{U}_w), \tag{3}$$

where (τ_{io}^{x}, τ_{io}^{y}) are zonal and meridional components of the ice-ocean surface stress, respectively; ρ_w is the water density (1026 kg m^{-3}); $C_{D,io}$ is the drag coefficient between ocean and ice, $\mathbf{U}_{\mathrm{ice}}$ is the observed sea ice velocity (Fowler et al., 2013); and $\mathbf{U}_{w}$ is water velocity (Häkkinen, 1986; Timmermann et al., 2009).

The drag coefficient $C_{D,io}$ between ice and water depends on the sea ice roughness (e.g. McPhee and Smith, 1976; Häkkinen, 1986; Leppäranta and Omstedt, 1990), the ice concentration, and length,

thickness and roughness of the sea ice plates (Lu et al., 2011). In the Arctic basin, drift ice is often rough due to ridging and may have a drag coefficient more than twice the value of un-deformed, level ice. In the Southern Ocean the ice is usually smoother. Another effect is the internal friction (e.g. Leppäranta and Hibler, 1985), which will be large e.g. if the ice cover becomes fast frozen to the coast. By comparing the observed veering and reduction in ice drift velocity compared to the 10 m wind, ball park estimates of an effective drag ice-ocean coefficient were obtained (Fig. S1 and Appendix). This estimate represents the two year (2011–12) average, taking into account effects of internal friction, and as can be seen (Fig. S1) it is highest close to the coast where the wintertime ice is fast and smaller close to the marginal ice zone where there are more freely flowing ice floes. Although the magnitude of the Ekman pumping in general increases with increasing value of $C_{D,io}$, the main result about the correlation between bottom temperature and Ekman pumping is not sensitive to the value of $C_{D,io}$ (Fig. S3; Appendix).

The surface water velocity $\mathbf{U_W}$ is needed in order to calculate the ice-ocean stress (Eq. (3)). Naturally, the water velocity is not known below the ice covered waters in the Amundsen Sea. A parameterization is obtained assuming that no other forces than the stress is acting on the water and that a full Ekman spiral develops below the ice, in which case the surface current velocities are given by Ekman (1905), Pond and Pickard (1983) and Yang (2006)

$$\begin{pmatrix} U_W^x \\ U_W^y \end{pmatrix} = \begin{pmatrix} \cos(\frac{\pi}{4}) & -\sin(\frac{\pi}{4}) \\ \sin(\frac{\pi}{4}) & \cos(\frac{\pi}{4}) \end{pmatrix} \begin{pmatrix} \frac{\tau_{io}^x}{\sqrt{\rho_w^2 f A_Z}} \\ \frac{\tau_{io}^y}{\sqrt{\rho_w^2 f A_Z}} \end{pmatrix}, \tag{4}$$

where A_Z is the vertical eddy viscosity (0.05 m^2/s), f [s^{-1}] is the Coriolis parameter and τ_{io}^x, τ_{io}^y are the surface stresses given by (3). We calculate the surface current velocity by iteration of Eqs. (3)–(4) until they converge, starting at $\mathbf{U_W = 0}$ in the first iteration. The sensitivity of the results to ocean current velocity was tested by comparing the obtained Ekman pumping using Eq. (3) with that obtained using $\mathbf{U_W = 0}$, and the difference was minor (Fig. S3).

Given the ice-ocean drag coefficient and the ocean surface velocity the surface stress is computed as a combination of ice-ocean and air-ocean stress according to

$$\tau_o = A\tau_{io} + (1 - A)\tau_{ao}, \tag{5}$$

where A is portion of area covered by sea ice (Yang, 2006; Timmermann et al., 2009). The Ekman pumping velocity w_E is then given by the curl of the surface stress (Harrison, 1989; Enriquez and Friehe, 1995), i.e.

$$w_E = \frac{1}{\rho_w f}\left(\frac{\partial \tau_o^y}{\partial x} - \frac{\partial \tau_o^x}{\partial y}\right), \tag{6}$$

where ρ_w is the seawater density, and (τ_0^x, τ_0^y) is the surface stress in the

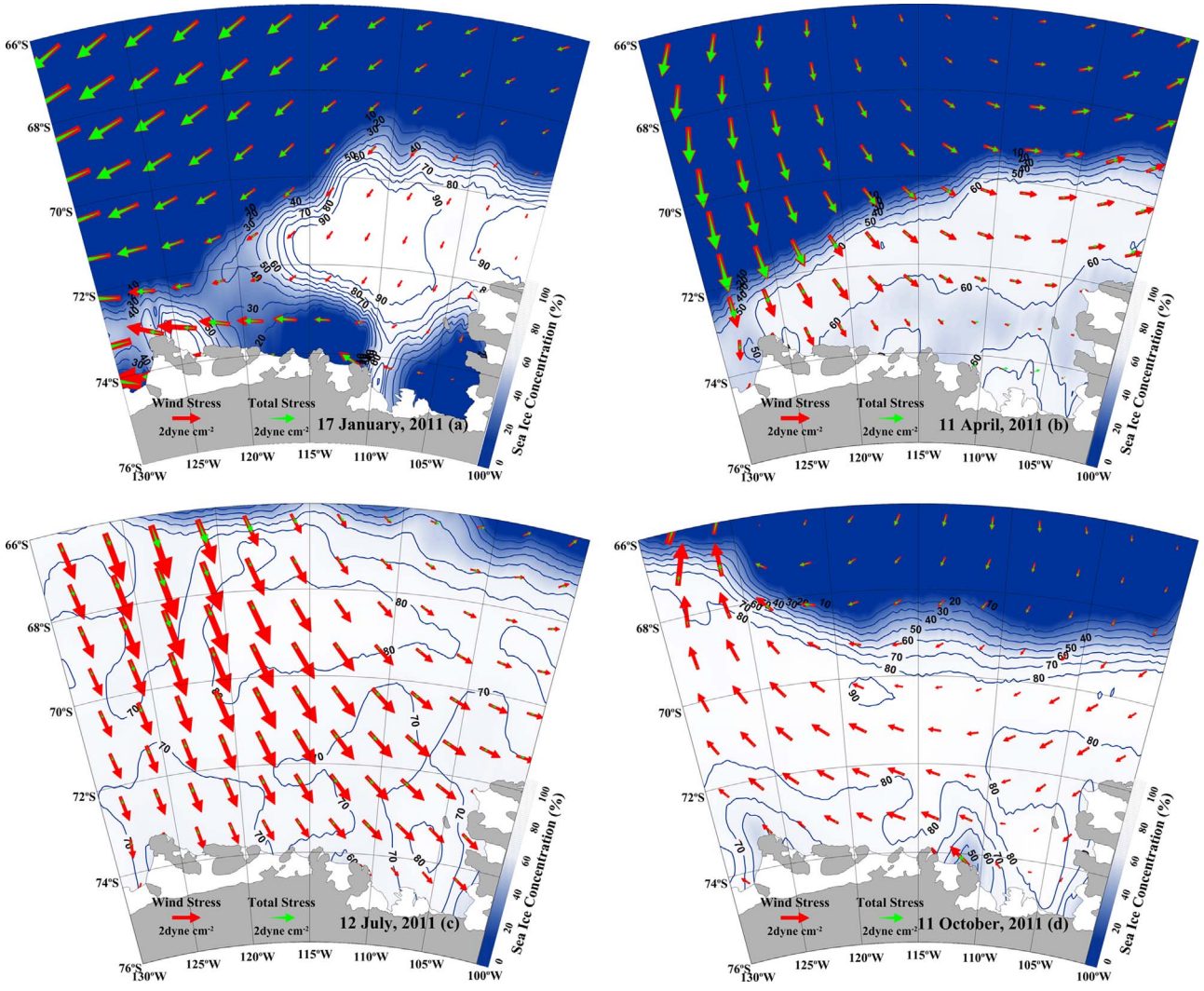

Fig. 4. Snapshots of the wind stress (red arrows), total stress (green arrows) and sea ice concentration (shading according to color bar) on (a) January 17, (b) April 11, (c) July 12, and (d) October 11, 2011. (For interpretation of the references to color in this figure legend, the reader is referred to the web version of this article.)

(*x, y*) direction given by (5). According to (6), Ekman pumping can be induced by horizontal variations in the wind field, in the sea ice drift, in the sea ice cover and combinations thereof.

Fig. 4 shows four snapshots of the surface stress from different seasons. In general, the stress is weaker below sea ice than in open water which induces a spatial gradient of the surface stress and Ekman pumping in the marginal ice zone (as pointed out in e.g. Häkkinen, 1986).

3. Results

Observations of potential temperature and salinity along the transect at 113–120°W, from 67°S to the front of the Dotson ice shelf (Fig. 2), show that the warmest water (> 2 °C) is found offshelf at about 300–500 m depth at 67°S (St. 29). A warm and salty tongue of CDW extends toward the ice shelf, becoming colder and fresher as it interacts with the surface water and/or subsurface glacial ice. Near the coast, the observed maximum temperature is 0.7 °C and the observed maximum salinity is 34.6 psu. In the sea ice covered stations (i.e. St. 07 and 08), the surface temperature was lower than that at the northern limit of the ice area. In the polynya (i.e. St. 09, 14 and 10), the sea surface temperature was higher (−0.8 to −0.4 °C) than that at the sea ice covered stations (e.g., St. 07 and 08). There is a slight elevation of the isotherms in the stations near the polynya boundary (stations 9 and 14) and near the northern ice edge (station 24). The red dashed line shows the 0 °C isotherm during the 2012 cruise, illustrating the large temporal variability in this area.

Fig. 3 shows daily averages of temperature, salinity, neutral density (Jackett and Trevor, 1997) and along-trough velocity (defined as velocity projected on 140° with positive values towards the ice shelf) at the mooring site. The thickness of the warm layer (identified here by the T=0 °C isotherm) and the bottom temperature both reach maxima in late summer and early autumn and minima in late winter and spring. The difference between the seasonal maximum and minimum in thickness is approximately 60–100 m and the difference between maximum and minimum bottom temperature is approximately 1 °C. A corresponding seasonal variation is seen in salinity (Fig. 3b), indicating that variations in temperature are not caused by atmospheric cooling (as this would not influence the salinity). In contrast to temperature and salinity, the seasonal variation of along-trough velocity (Fig. 3d) is relatively weak. The variability in velocity is dominated by barotropic fluctuations induced by the local wind (Wåhlin et al., 2013, 2016; Kalén et al., 2015). However, the local wind is not correlated with either warm layer thickness or bottom temperature (Wåhlin et al., 2013).

Snapshots of the sea ice concentration, wind stress (Eq. (1)), and total surface stress (Eq. (5)) for the four seasons are shown in Fig. 4. In ice covered regions there is a clear difference between the two calculations, with a leftward veering and a reduction in stress magnitude when sea ice is present. The magnitude and direction of surface stress hence change across the ice front indicating that the seasonal movement of the marginal ice zone is important for the Ekman

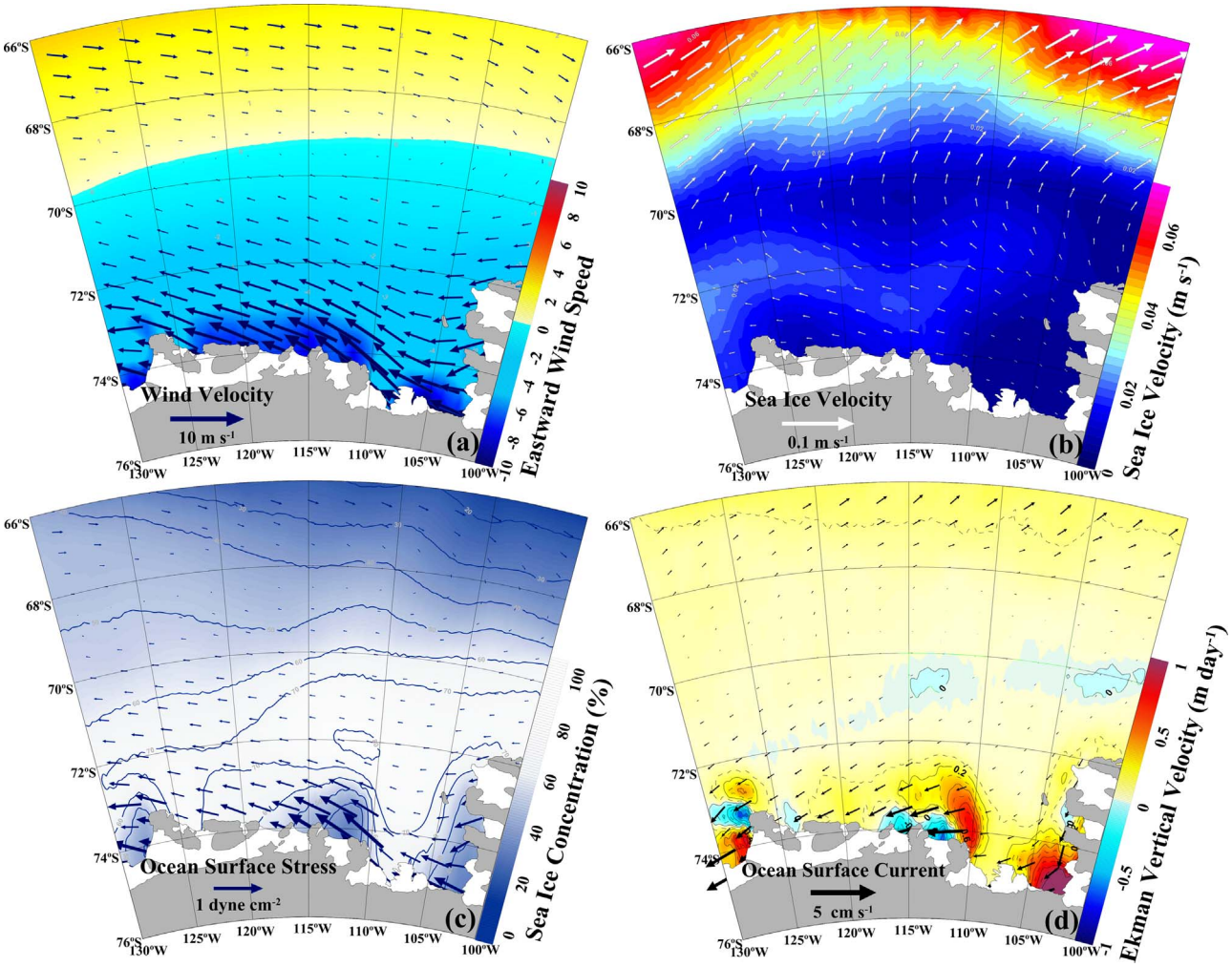

Fig. 5. Two-year (2010–2011) average (a) wind field, (b) sea ice velocity, (c) ocean surface stress (blue arrow) and sea ice concentration, (d) ocean surface current (black arrow) and Ekman vertical velocity (according to color bar). (For interpretation of the references to color in this figure legend, the reader is referred to the web version of this article.)

dynamics. This can be seen at the marginal ice zone in spring and fall and at the northward boundary of the polynya in spring. Due to the ice effects there is a pronounced lateral variation of the surface stress even though the wind field is comparatively homogenous across the area. This could potentially generate the observed seasonal variation MCDW layer thickness.

Fig. 5 shows 2 years temporal average (based on data from 2010 to 2011) of wind, sea ice velocity, ocean surface stress, ice concentration and surface current velocity (calculated according to (4)). The latitudinal variation of the average wind (Fig. 5a) shows eastward wind north of 69°S and westward wind south of 69°S. In similarity with the wind field there is a large-scale meridional variation of the ice drift. Close to the coast the average ice drift is small (Fig. 5b) reflecting the fact that the ice is fast frozen to the coast there in winter. The surface stress (Fig. 5c) shows a maximum and a strong westward component (1.5 dyne cm^{-2}) in front of Dotson Ice Shelf, where the sea ice concentration was less than 35%. The smallest surface stress (0.02 dyne cm^{-2}) is coinciding with highest sea ice concentration around 68.5°S. A large area of positive Ekman pumping (> 0.1 m day^{-1}) is located around 66°S. Between 68°S and 71°S, where the average sea ice concentration exceeds 40%, the stress curl is less than 0.1 m day^{-1}. In the polynyas the wind is mainly westward and the Ekman pumping is positive due to the combination of winds and the sea ice cover. In the western parts of the polynya and along the coastline, negative Ekman pumping is found.

Both wind stress curl and sea ice concentration have a pronounced seasonal variation, illustrated in Fig. 6 where seasonal averages (based on the 2 year record) of surface stress, sea ice concentration and Ekman pumping are shown. During spring, positive Ekman pumping appears north of the shelf break, possibly causing the observed lifting of isohalines there (Fig. 2), as suggested by previous studies (e.g., Jacobs et al., 2012). During summer the area of strong positive Ekman pumping stretches to the shelf break as the polynya expands northward, meeting the area of negative Ekman pumping associated with the marginal ice zone. During winter the shelf break region is covered with more or less land-fast ice and has very small Ekman pumping.

In order to investigate the effect of Ekman pumping on the bottom temperature at the mooring site, a correlation lag-plot was constructed of the correlation between the 29-day (lunar month) running average of Ekman pumping and bottom temperature at the mooring site (Fig. 7a). Neighboring grid points show similar correlation-lag dependency, i.e. with the strongest correlation in a broad peak centered around 46 days time lag. This fits qualitatively with the observation that the average velocity at the mooring is 3.5 cm s^{-1} (Kalen et al., 2015): During 46 days the water travels on average 120 km which is the rough distance between the mooring and the shelf break. The statistically significant negative correlation that is seen around 80–90 days lag is likely a reflection of the seasonal cycle, i.e. a mirror correlation that occurs approximately half a year shifted in time (i.e. the wintertime minimum happening half a year after the summertime maximum). The horizontal distribution of the correlation is shown in Fig. 7b. Inner areas of solid and dashed lines indicate that the correlation was statistically significant using 99% (solid) and 95% (dashed) confidence interval. Significant correlation was found at the Dotson Trough near the trough mouth, the shelf break and the northern boundary of the Amundsen Polynya. Positive significant correlation was found also in front of Pine Island Glacier and Getz Ice Shelf. Negative significant correlation was found at sea ice covered areas west of the polynyas and at the marginal ice zone. These spatial patterns are likely caused by the large-scale wind field (Fig. 5) in combination with the sea ice distribution. The northern edge of the polynya is associated with upwelling for eastward winds and downwelling for westward winds, while the northern sea ice edge is associated with downwelling for eastward winds and upwelling for westward. Therefor the polynya regions and the area north of the shelf break are expected to have opposite signs of correlation. Coastal regions without polynyas (e.g. west of the Amundsen Polynya) is associated with downwelling for eastward winds and upwelling for westward, i.e. same sign correlation as the sea ice edge north of the shelf break.

Fig. 8 shows the time development of Ekman pumping at the mooring site together with the bottom temperature. The increase in bottom temperature is preceded by a series of events with high Ekman pumping. These events (in March, April and May of 2010 and 2011) appear to press warm deep water up onto the shelf in cascades during which time the temperature of the water in Dotson Trough increases. Also shown in Fig. 8c is the accumulated Ekman pumping, lagged 46 days, which appears to follow the temperature curve closely during the warming phase. The quiet seasons (fall and winter) when there is less warm water pumped up onto the shelf are characterized by a gradual cooling of the bottom water, not correlated to the Ekman pumping or to its cumulative sum. A possible mechanism explaining why the correlation is strong at the shelf break and at the northern boundary of the polynya is sketched in Fig. 9. The northward expansion of the polynya in combination with westward winds causes an upwelling as the polynya boundary approaches the shelf break, lifting deep warm water from offshore over the shelf break after which it flows southward in the deep trough.

4. Discussion

The observational results obtained here suggest that in addition to the barotropic fluctuating clockwise flow that has been observed in the deep troughs on the Amundsen Sea (Arneborg et al., 2012; Assmann et al., 2013; Wåhlin et al., 2013; 2015; Ha et al., 2014; Nakayama et al., 2013), there is a seasonally varying Ekman transport at the shelf break that moves warm and salty MCDW up onto the continental shelf. The thickness of the warm layer reaches maximum in late summer and fall which coincides in time with when the northern boundary of the polynya is near the shelf break. Both the bottom temperature and the position of the 0 °C isotherm (Fig. 3) showed a similar seasonal variation, with maximum in late summer and minimum in late winter/spring. The observed meridional variation of isohalines and isotherms north of the shelf break (Fig. 2), with a local lifting of isotherms near the marginal ice zone, indicates that processes at the sea ice edge can be responsible for moving warm water onto the shelf. The fact that currents on the shelf lack a seasonal signal and is not correlating with the bottom temperature in the deep troughs (Wåhlin et al., 2013; Assmann et al., 2013) implies that it is the surface forcing rather than ocean circulation dynamics that causes the seasonal variation of the warm layer.

Internal ice dynamics and lateral variations of the ice-ocean drag coefficient makes any parameterization of the ice-ocean drag (and hence the Ekman transport below sea ice) highly uncertain. An estimate of the effective ice-ocean drag coefficient (Fig. S1) was nonetheless obtained by using the observed veering and reduction in ice drift velocity compared to the 10 m wind. This showed a large lateral variation likely reflecting the fact that the ice is fast close to the coast and freely moving further north. By combining the wind-driven surface stress with the one parameterized from the moving sea ice an Ekman transport for the whole region was obtained. As the sea ice edge migrated over the shelf break this gave rise to intermittent pulses of Ekman pumping (exceeding 1 m day^{-1} in January and February, Fig. 8), coinciding in time with the build-up of the thicker and warmer layer of MCDW in Dotson Trough, and a statistically significant positive correlation between the shelf break Ekman pumping and the bottom temperature in Dotson Trough (Fig. 7). Such a seasonal variation is not seen in surface stress parameterizations based on only wind (e.g. Wåhlin et al., 2013), which is in contrast to model results (e.g. Thoma et al., 2008; Steig et al., 2012) and indicates that the modulation of surface stress by sea ice is changing the seasonal surface forcing in this region. However, it should be stressed that there are large uncertainties with the present parameterization of surface stress, in particular with

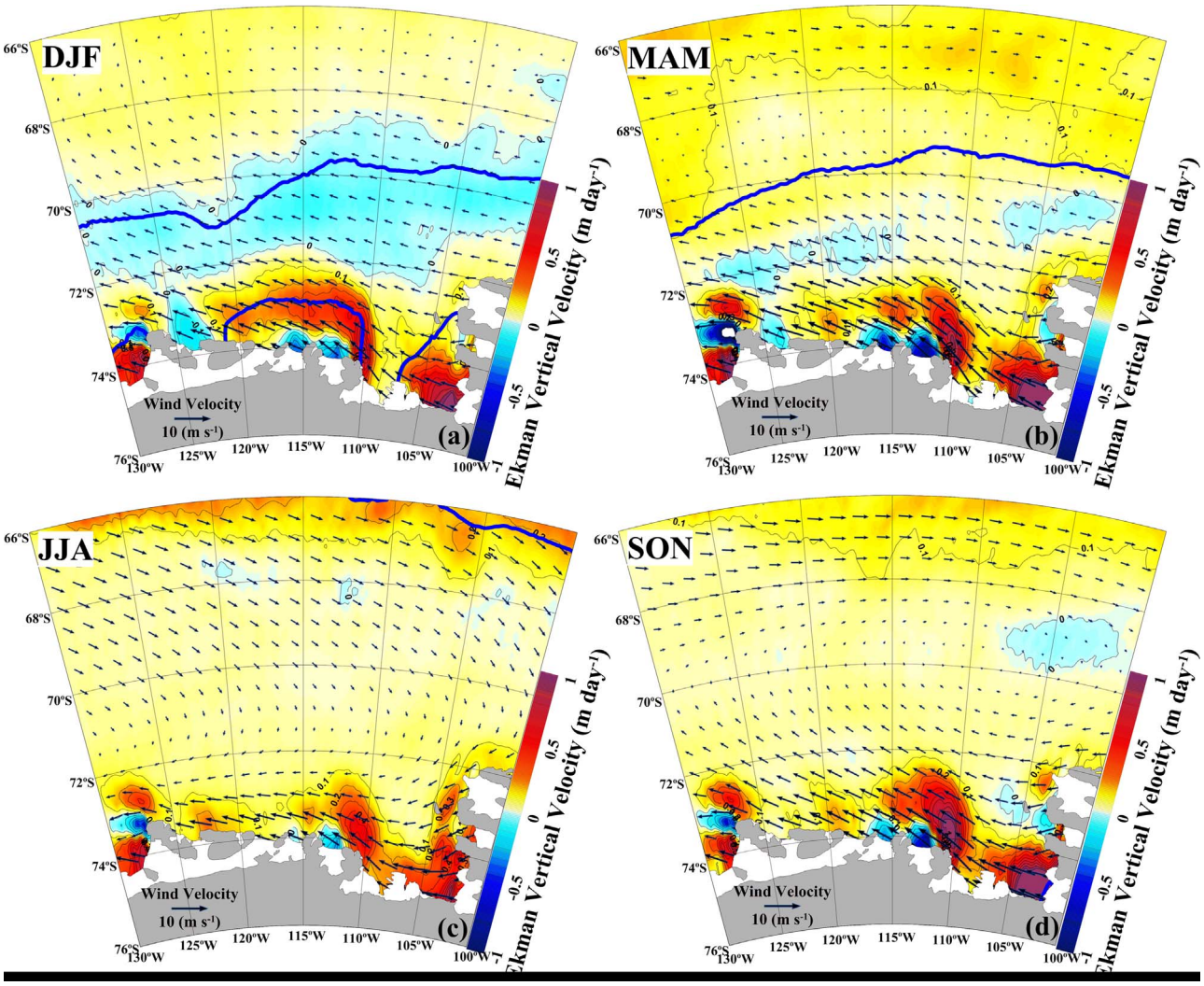

Fig. 6. Seasonal averages of wind field (arrows), Ekman vertical velocity (according to color bar), and 30% sea ice concentration (blue line), measured during 2010–2011 for the months (a) December–January–February, (b) March–April–May, (c) June–July–August, and (d) September–October–November. (For interpretation of the references to color in this figure legend, the reader is referred to the web version of this article.)

the ice-ocean stress. The sea ice drift and ice concentration are based on data of better resolution and quality than the wind model. This means that any variation of stress to the ocean that is parameterized based on ice data is automatically going to have larger gradients and hence larger Ekman pumping associated with it. Another factor is that the wind data over sea ice has larger errors than wind data over open water (Bumbaco et al., 2014). It should however be noted that the regions of largest Ekman pumping (e.g. the polynya and next to the coast) are not the regions with highest correlation with bottom temperature. Highest correlation is found at the outer shelf region which does not have unusually large sea ice gradients nor sea ice concentration. These properties speak against the results being an artefact of the usage of two different data sets. The similarity between time series of Ekman pumping obtained using a range of different ice-ocean drag coefficients (Fig. S3) also suggests that the result is fairly robust, and that ice-modulated Ekman pumping at the shelf break is indeed a mechanism that brings warm CDW across the shelf break in a seasonally varying pattern. The main effect of the sea ice cover for this region and time period appears to be that it shelters the ocean from the wind and gives the sea ice covered regions smaller stress and smaller Ekman transport compared to ice-free regions.

Since the Ekman pumping appears to be modulated by the position of the migrating ice edge, it explains why previous studies found no correlation between eastward wind and bottom temperature in Dotson Trough (Wåhlin et al., 2013). It is clear from the obtained results that the wind alone cannot explain the observed seasonality, and that sea ice needs to be taken into account to obtain more accurate surface stress in ice covered regions. A seasonal variation with maximum thickness of the warm bottom layer in late summer/fall has also been observed in Prydz Bay (Herraiz-Borreguero et al., 2015), suggesting that the mechanism can be active also there. Ekman pumping caused by seasonal migration of the marginal ice zone has also been observed in the Arctic (e.g. Häkkinen, 1986; Carmack and Chapman, 2003).

The emerging picture of the circulation on the Amundsen continental shelf is only partly recaptured by existing models. In Assmann et al. (2013) a positive correlation between modeled along-shelf velocity at the shelf break and inflow velocity in the trough was found, similar to the idealized study by St. Laurent et al. (2012). However, in contrast to the present observational findings, both Dinniman et al. (2011) and Steig et al. (2012) have maximum warm layer thicknesses in July–October, correlated with the wind stress at the shelf break (see also Thoma et al. (2008)). The modeled thickness of the warm layer hence appears to be less well reproduced by models, and the argument that increased eastward wind would flood the Antarctic shelf regions with warm water and increase ice shelf melt (e.g. Steig et al., 2012; Pritchard et al., 2012; Pike et al., 2013) does not find support in the present data series. Since there is substantial short-term variability in the ocean velocity field that is not coupled to the bottom temperature

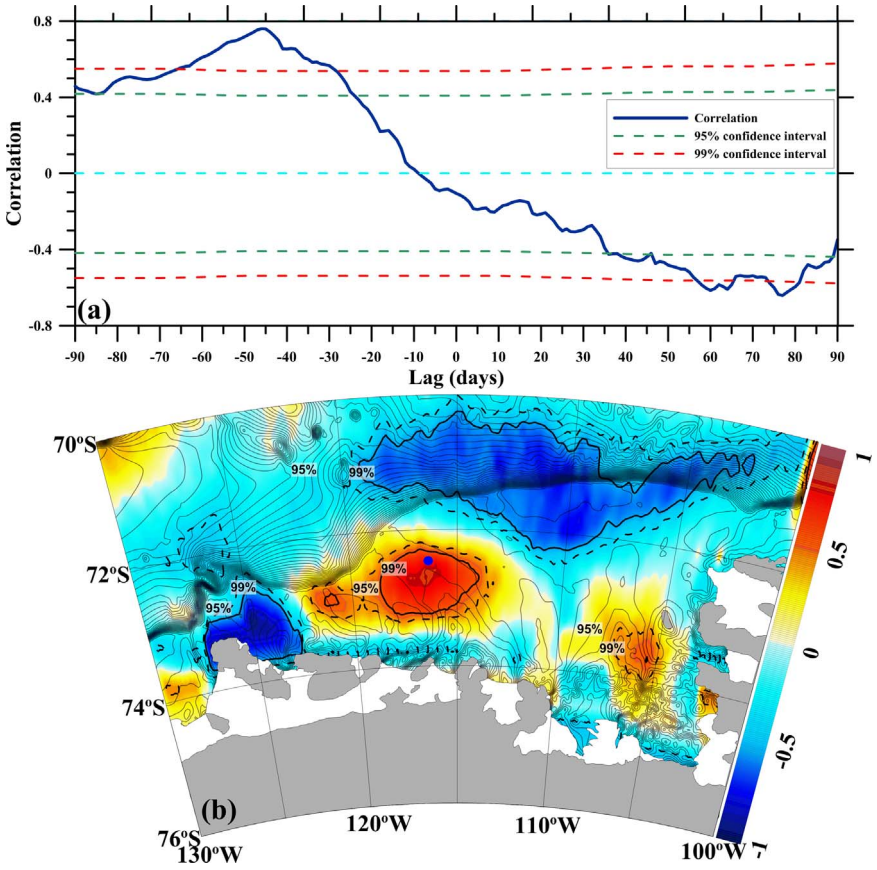

Fig. 7. (a) Correlation-lag plot between Ekman pumping and bottom temperature (both 29 day averages) at mooring site (blue dot inb). Solid line indicates correlation; dashed lines indicate 99% and 95% confidence intervals. Negative lag means that Ekman pumping is shifted ahead in time. (b) Spatial distribution of the strongest correlation (according to color bar), bottom temperature and Ekman pumping (both 29 day averages). Inner areas of solid and dashed contours indicate that the correlation was statistically significant using 99% and 95% confidence interval. (For interpretation of the references to color in this figure legend, the reader is referred to the web version of this article.)

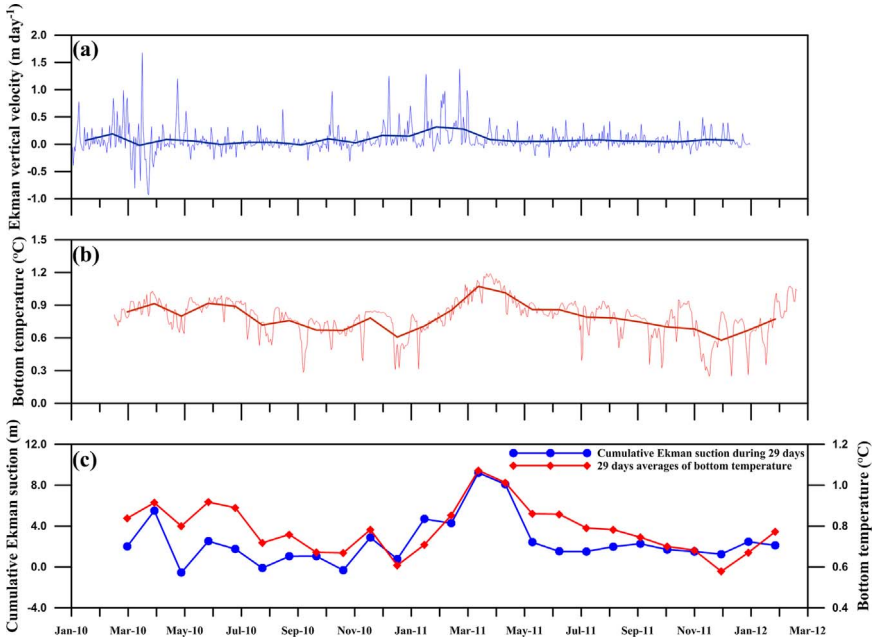

Fig. 8. Time series of Ekman pumping and bottom temperature at mooring site. (a) Daily (thin line) and 29 day average (thick line) Ekman pumping (b) Daily (thin line) and 29 day average (thick line) bottom temperature (c) Accumulated Ekman pumping with 46 days lag (blue) together with bottom temperature (red line) (both 29 day average values). (For interpretation of the references to color in this figure legend, the reader is referred to the web version of this article.)

(e.g. Wåhlin et al., 2016; Wåhlin et al., 2013) and the continental shelf is deep (400–800 m) it is not likely that there are any systematic effects of the continental shelf bathymetry like there could be in the Arctic. It is believed that the observation that the shelf break is a key region where wind and sea ice dynamics help to pump water up onto the shelf is due to the tendency of the sea ice edge to be close to the shelf break

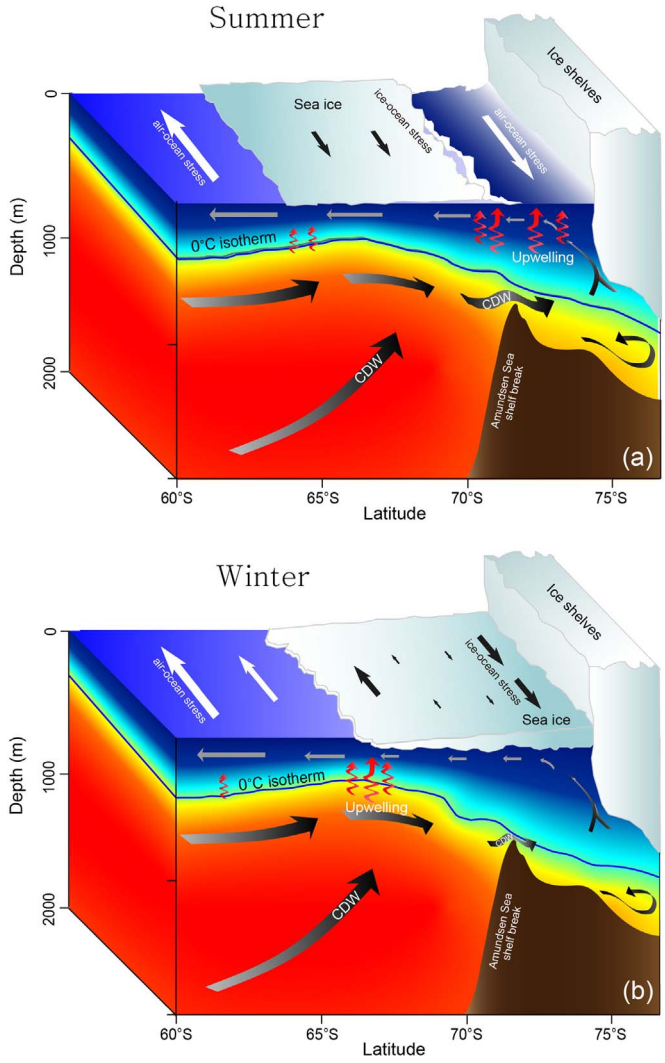

Fig. 9. Schematic diagrams explaining the circulation of deep warm water and its relationship with wind forcing and sea ice distribution during austral summer (a) and winter (b) in the Amundsen Sea.

during late summer and fall.

Acknowledgments

We would like to thank C. S. Hong, H. J. Lee and L. Arneborg for mooring data acquisition and analysis. We also thank M. Tschudi for providing the Polar Pathfinder daily 25 km EASE-Grid sea ice motion data. This work was supported by grants from the K-Polar Program (Grants PP13020 and PP14020) of KOPRI, the National Research Foundation of Korea (No. 2015K2A3A1000201), and the Swedish Research Council (2011-5263).

Appendix A. Parameterization of ice-ocean drag coefficient and ocean current velocity

In this appendix the parameterizations used for ice-ocean drag coefficient and for the ocean current velocity is described, and some estimates of the sensitivity of the results to these quantities is provided. The drag coefficient is based on observed veering and speed reduction of sea ice compared to wind, according to the following:

According to the free drift sea ice motion is determined by the balance of wind and water stress and the Coriolis force,

$$\rho_a C_{D,ai}|W_{10}|W_{10}+R(\theta_w)\rho_w C_{D,io}|U_w-U_{ice}|(U_w-U_{ice})+R\left(\frac{\pi}{2}\right)\rho_{ice} hf(U_w-U_{ice})=0 \quad \text{(A1)}$$

where W_{10}, U_w, and U_{ice} are surface wind, ocean current, and sea ice velocities; ρ_a, ρ_w, and ρ_{ice} are densities of air, water, and sea ice; h is ice thickness; f is the Coriolis parameter; $C_{D,ai}=1.6\times10^{-3}$ (e.g. Andreas, 1995; Koentopp et al., 2005) is air-ice drag coefficient, and the rotation matrix $R(\theta)$ is given by

$$R(\theta)=\begin{pmatrix}\cos\theta & -\sin\theta\\ \sin\theta & \cos\theta\end{pmatrix}. \quad \text{(A2)}$$

Generally, the sea ice velocity of free drift can be expressed as

$$U_{ice}=\alpha R(-\theta)W_{10}+U_w, \quad \text{(A3)}$$

where α is the wind factor and θ is the angle between $(U_{ice}-U_w)$ and W_{10}. In order to estimate the ice-ocean drag coefficient $C_{D,io}$, it is assumed that

$U_w << U_{ice}$. Then (A1) and (A3) can be simplified and combined to the following (Lu et al., 2016):

$$\alpha^4+N_a^2R_O^2\alpha^2-N_a^4=0, \tag{A4}$$

where N_a is the Nansen Number and R_o the ice Rossby Number defined as

$$N_a=\sqrt{\frac{\rho_a C_{D,ai}}{\rho_w C_{D,io}}} \text{ and} R_o=\frac{\rho_{ice} Hf}{\rho_w C_{D,io} N_a |W_{10}|} \quad , \tag{A5}$$

Using (A4) and (A5), the wind factor and angle can be expressed in terms of R_o and N_a

$$\alpha=N_a\sqrt{\frac{\sqrt{R_o^4+4}-R_o^2}{2}} \text{ and} \theta=arctan\left(\frac{N_a R_o}{\alpha}\right)=arctan\left(\frac{1}{\sqrt{\sqrt{\frac{1}{4}+\frac{1}{R_o^4}}-\frac{1}{2}}}\right) \tag{A6}$$

Inverting (A6) gives the following expressions for N_a and R_o as functions of θ and α,

$$N_a=\frac{\alpha}{\sqrt{\frac{1}{\sqrt{\left(\frac{1}{tan^2\theta}+\frac{1}{2}\right)^2-\frac{1}{4}}}+4-\frac{1}{\sqrt{\left(\frac{1}{tan^2\theta}+\frac{1}{2}\right)^2-\frac{1}{4}}}}{2}}} \text{ and} R_o=\frac{1}{\sqrt{\left(\frac{1}{tan^2\theta}+\frac{1}{2}\right)^2-\frac{1}{4}}} \tag{A7}$$

The wind factor and angle can also be calculated from data according to (e.g. Kimura (2004)),

$$\theta=arctan\left(\frac{\sum W_{10}^x{}' U_{ice}^y{}' - \sum W_{10}^y{}' U_{ice}^x{}'}{\sum W_{10}^x{}' U_{ice}^x{}' - \sum W_{10}^y{}' U_{ice}^y{}'}\right) \alpha=\frac{\cos(\theta)\sum W_{10}^x{}' U_{ice}^x{}' + \sin(\theta)\sum W_{10}^y{}' U_{ice}^x{}' - \sin(\theta)\sum W_{10}^x{}' U_{ice}^y{}' + \cos(\theta)\sum W_{10}^y{}' U_{ice}^y{}'}{\sum U_{ice}^x{}^2 - \sum U_{ice}^y{}^2}, \tag{A8}$$

where $W_{10}^x{}'$, $W_{10}^y{}'$, $U_{ice}^x{}'$, and $U_{ice}^y{}'$ are anomalies defined by $(W_{10}^x-\overline{W_{10}^x})$, $(W_{10}^y-\overline{W_{10}^y})$, $(U_{ice}^x-\overline{U_{ice}^x})$, and $(U_{ice}^y-\overline{U_{ice}^y})$ and $\overline{W_{10}^x}$, $\overline{W_{10}^y}$, $\overline{U_{ice}^x}$, and $\overline{U_{ice}^y}$ are mean values of 10 m wind and sea ice velocity of zonal and meridional direction, respectively. Using (A8) in (A7) and (A6) allows calculating the average $C_{D,io}$ in the region based on the two years of wind and ice drift data (assuming a horizontally homogeneous $C_{D,ai}=1.6\times10^{-3}$). This has been done in Fig. S1.

The sensitivity of the results on the magnitude of $C_{D,io}$ were tested by using three different constant $C_{D,io}$ ranging from 0.5×10^{-3} to 4.5×10^{-3}, in addition to the horizontally varying one in Fig. S1. Fig. S3 shows time series of the four different mooring site Ekman pumping and accumulated transports thus obtained. Although the resulting Ekman pumping was somewhat larger for large $C_{D,io}$ the correlation between Ekman pumping and bottom temperature was only marginally affected (Fig. S3). Also included in Fig. S3 is a comparison between the Ekman pumping obtained using only wind, using a combination of wind and sea ice drift assuming that the ocean current velocity is zero and using wind and sea ice drift assuming that the ocean current velocity is given by expression (4). As can be seen the parameterization of the ocean current velocity gives minor effects compared to the inclusion of the sea ice drift.

Appendix B. Supporting information

Supplementary data associated with this article can be found in the online version at doi:10.1016/j.csr.2016.09.005.

References

Andreas, E.L., 1995. Air-ice drag coefficients in the western Weddell Sea: 2. A model based on form drag and drifting snow. J. Geophys. Res.: Oceans 100 (C3), 4833–4843.

Arneborg, L., Wåhlin, A.K., Björk, G., Liljebladh, B., Orsi, A.H., 2012. Persistent inflow of warm water onto the central Amundsen shelf. Nat. Geosci. 5 (12), 876–880.

Assmann, K.M., Jenkins, A., Shoosmith, D.R., Walker, D.P., Jacobs, S.S., Nicholls, K.W., 2013. Variability of circumpolar deep water transport onto the Amundsen Sea Continental shelf through a shelf break trough. J. Geophys. Res.: Oceans 118 (12), 6603–6620.

Bindschadler, R., 2006. The environment and evolution of the West Antarctic ice sheet: setting the stage. Philos. Trans. R. Soc. A: Math. Phys. Eng. Sci. 364 (1844), 1583–1605.

Bumbaco, K.A., Hakim, G.J., Mauger, G.S., Hryniw, N., Steig, E.J., 2014. Evaluating the Antarctic Observational Network with the Antarctic Mesoscale Prediction System (AMPS). Mon. Weather Rev. 142 (10), 3847–3859.

Carmack, E., Chapman, D.C., 2003. Wind-driven shelf/basin exchange on an Arctic shelf: the joint roles of ice cover extent and shelf-break bathymetry. Geophys. Res. Lett. 30 (14).

Cavalieri, D.J., Parkinson, C.L., Gloersen, P., Zwally, H., 1996. Sea Ice Concentrations from Nimbus-7 SMMR and DMSP SSM/I-SSMIS Passive Microwave Data, years 2010–2011. NASA DAAC at the Natl. Snow and Ice Data Cent., Boulder, Colo. (Updated yearly).

Dinniman, M.S., Klinck, J.M., Smith, W.O., 2011. A model study of circumpolar deep water on the West Antarctic Peninsula and Ross Sea continental shelves. Deep Sea Res. Part II: Top. Stud. Oceanogr. 58 (13), 1508–1523.

Dutton, A., Carlson, A.E., Long, A.J., Milne, G.A., Clark, P.U., DeConto, R., Horton, B.P., Rahmstorf, M.E., Raymo, M.E., 2015. Sea-level rise due to polar ice-sheet mass loss during past warm periods. Science 349 (6244), aaa4019.

Ekman, V.W., 1905. On the influence of the earth's rotation on ocean currents. Ark. Mat. Astron. Fys. 2, 1–53.

Enriquez, A.G., Friehe, C.A., 1995. Effects of wind stress and wind stress curl variability on coastal upwelling. J. Phys. Oceanogr. 25 (7), 1651–1671.

Foreman, M.G.G., 1979. Manual for Tidal Heights Analysis and Prediction. Institute of Ocean Sciences, Patricia Bay.

Fowler, C., Emery, W., Tschudi, M., 2013. Polar Pathfinder Daily 25 km EASE-Grid Sea Ice Motion Vectors. Version 2. 2010-2011. NASA DAAC at the National Snow and Ice Data Center, Boulder, Colorado USA.

Ha, H.K., Wåhlin, A.K., Kim, T.W., Lee, S.H., Lee, J.H., Lee, H.J., Hong, C.S., Arneborg, L., Björk, G., Kalén, O., 2014. Circulation and modification of warm deep water on the central Amundsen Shelf. J. Phys. Oceanogr. 44 (5), 1493–1501.

Häkkinen, S., 1986. Coupled ice-ocean dynamics in the marginal ice zones: upwelling/downwelling and eddy generation. J. Geophys. Res.: Oceans (1978–2012), 91(C1) 819–832.

Harrison, D.E., 1989. On climatological monthly mean wind stress and wind stress curl fields over the world ocean. J. Clim. 2 (1), 57–70.

Hawkings, J.R., Wadham, J.L., Tranter, M., Raiswell, R., Benning, L.G., Statham, P.J., Tedstone, A., Nienow, P., Lee, K., Telling, J., 2014. Ice sheets as a significant source of highly reactive nanoparticulate iron to the oceans. Nat. Commun. 5.

Herraiz-Borreguero, L., Coleman, R., Allison, I., Rintoul, S.R., Craven, M., Williams, G.D., 2015. Circulation of modified circumpolar deep water and basal melt beneath the Amery Ice Shelf, East Antarctica. J. Geophys. Res.: Oceans.

Intergovernmental Panel on Climate Change (IPCC), 2013. Climate Change 2013: The Physical Science Basis. Stocker, T., et al. (Eds.). Cambridge University Press, Cambridge, U.K., p. 2216.

Jackett, David R., Trevor, J. Mc.Dougall, 1997. A neutral density variable for the World's oceans. J. Phys. Oceanogr. 27, 237–263. http://dx.doi.org/10.1175/1520-0485(1997)0272.0.CO;2.

Jacobs, S., Jenkins, A., Hellmer, H., Giulivi, C., Nitsche, F., Huber, B., Guerrero, R., 2012. The Amundsen Sea and the Antarctic ice sheet. Oceanography 25 (3), 154–163.

Jacobs, S.S., Jenkins, A., Giulivi, C.F., Dutrieux, P., 2011. Stronger ocean circulation and increased melting under Pine Island Glacier ice shelf. Nat. Geosci. 4 (8), 519–523.

Jenkins, A., Dutrieux, P., Jacobs, S.S., McPhail, S.D., Perrett, J.R., Webb, A.T., White, D.,

2010. Observations beneath Pine Island Glacier in West Antarctica and implications for its retreat. Nat. Geosci. 3 (7), 468–472.
Kalén, O., Assmann, K.M., Wåhlin, A.K., Ha, H.K., Kim, T.W., Lee, S.H., 2015. Is the oceanic heat flux on the central Amundsen sea shelf caused by barotropic or baroclinic currents? Deep Sea Research Part II: Topical Studies in Oceanography.
Kimura, N., 2004. Notes and correspondence sea ice motion in response to surface wind and ocean currents in the Southern Ocean. J. Meteorol. Soc. Jpn. 82 (4), 1223–1231.
Koentopp, M., Eisen, O., Kottmeier, C., Padman, L., Lemke, P., 2005. Influence of tides on sea ice in the Weddell sea: investigations with a high-resolution dynamic-thermodynamic sea ice model. J. Geophys. Res.: Oceans 110 (C2).
Large, W.G., Pond, S., 1981. Open ocean momentum flux measurements in moderate to strong winds. J. Phys. Oceanogr. 11 (3), 324–336.
Leppäranta, M., Hibler, W.D., 1985. The role of plastic ice interaction in marginal ice zone dynamics. J. Geophys. Res.: Oceans 90 (C6), (1978–2012).
Leppäranta, M., Omstedt, A., 1990. Dynamic coupling of sea ice and water for an ice field with free boundaries. Tellus A 42 (4), 482–495.
Lu, P., Li, Z., Han, H., 2016. Introduction of parameterized sea ice drag coefficients into ice free-drift modeling. Acta Oceanol. Sin. 35 (1), 53–59.
Lu, P., Li, Z., Cheng, B., Leppäranta, M., 2011. A parameterization of the ice-ocean drag coefficient. J. Geophys. Res.: Oceans 116 (C7), (1978–2012).
McPhee, M.G., Smith, J.D., 1976. Measurements of the turbulent boundary layer under pack ice. J. Phys. Oceanogr. 6 (5), 696–711.
Menviel, L., Timmermann, A., Timm, O.E., Mouchet, A., 2010. Climate and biogeochemical response to a rapid melting of the West Antarctic ice sheet during interglacials and implications for future climate. Paleoceanography 25, 4.
Nakayama, Y., Schröder, M., Hellmer, H.H., 2013. From circumpolar deep water to the glacial meltwater plume on the eastern Amundsen shelf. Deep Sea Res. Part I: Oceanogr. Res. Pap. 77, 50–62.
Paolo, F.S., Fricker, H.A., Padman, L., 2015. Volume loss from Antarctic ice shelves is accelerating. Science 348 (6232), 327–331.
Pawlowicz, R., Beardsley, B., Lentz, S., 2002. Classical tidal harmonic analysis including error estimates in MATLAB using T_TIDE. Comput. Geosci. 28 (8), 929–937.
Pike, J., Swann, G.E., Leng, M.J., Snelling, A.M., 2013. Glacial discharge along the west Antarctic Peninsula during the Holocene. Nat. Geosci. 6 (3), 199–202.
Pond, S., Pickard, G.L., 1983. Introductory Dynamical Oceanography. Gulf Professional Publishing.
Pritchard, H.D., Ligtenberg, S.R.M., Fricker, H.A., Vaughan, D.G., Van den Broeke, M.R., Padman, L., 2012. Antarctic ice-sheet loss driven by basal melting of ice shelves. Nature 484 (7395), 502–505.
Rignot, E., Jacobs, S.S., 2002. Rapid bottom melting widespread near Antarctic ice sheet grounding lines. Science 296 (5575), 2020–2023.
Rignot, E., Bamber, J.L., Van Den Broeke, M.R., Davis, C., Li, Y., Van De Berg, W.J., Van Meijgaard, E., 2008. Recent Antarctic ice mass loss from radar interferometry and regional climate modelling. Nat. Geosci. 1 (2), 106–110.
Schulze, L.M., Pickart, R.S., 2012. Seasonal variation of upwelling in the Alaskan Beaufort Sea: Impact of sea ice cover. J. Geophys. Res.: Oceans 117 (C6), (1978–2012).
St. Laurent, L., Naveira Garabato, A.C., Ledwell, J.R., Thurnherr, A.M., Toole, J.M., Watson, A.J., 2012. Turbulence and diapycnal mixing in Drake Passage. J. Phys. Oceanogr. 42 (12), 2143–2152.
Steig, E.J., Ding, Q., Battisti, D.S., Jenkins, A., 2012. Tropical forcing of Circumpolar Deep Water inflow and outlet glacier thinning in the Amundsen Sea Embayment, West Antarctica. Ann. Glaciol. 53 (60), 19–28.
Thoma, M., Jenkins, A., Holland, D., Jacobs, S., 2008. Modelling circumpolar deep water intrusions on the Amundsen Sea continental shelf, Antarctica. Geophys. Res. Lett. 35 (18).
Timmermann, R., Danilov, S., Schröter, J., Böning, C., Sidorenko, D., Rollenhagen, K., 2009. Ocean circulation and sea ice distribution in a finite element global sea ice–ocean model. Ocean Model. 27 (3), 114–129.
Wåhlin, A.K., Yuan, X., Björk, G., Nohr, C., 2010. Inflow of warm circumpolar deep water in the central amundsen shelf. J. Phys. Oceanogr. 40 (6), 1427–1434.
Wåhlin, A.K., Muench, R.D., Arneborg, L., Björk, G., Ha, H.K., Lee, S.H., Alsén, H., 2012. Some implications of Ekman layer dynamics for cross-shelf exchange in the Amundsen Sea. J. Phys. Oceanogr. 42 (9), 1461–1474.
Wåhlin, A.K., Kalén, O., Arneborg, L., Björk, G., Carvajal, G.K., Ha, H.K., Kim, T.W., Lee, S.H., Stranne, C., 2013. Variability of warm deep water inflow in a submarine trough on the Amundsen Sea shelf. J. Phys. Oceanogr. 43 (10), 2054–2070.
Wåhlin, A.K., Kalén, O., Assmann, K., Darelius, E., Ha, H.K., Lee, S.H., 2016. Sub-inertial oscillations on the central Amundsen Shelf. J. Phys. Oceanogr. 46 (9), 2573–2582. http://dx.doi.org/10.1175/JPO-D-14-0257.1.
Walker, D.P., Brandon, M.A., Jenkins, A., Allen, J.T., Dowdeswell, J.A., Evans, J., 2007. Oceanic heat transport onto the Amundsen Sea shelf through a submarine glacial trough. Geophys. Res. Lett. 34 (2).
Yang, J., 2006. The seasonal variability of the Arctic Ocean Ekman transport and its role in the mixed layer heat and salt fluxes. J. Clim. 19 (20), 5366–5387.